Draft version October 4, 2013
Preprint typeset using LaTeX style emulateapj v. 11/10/09

QUANTITATIVE ESTIMATES OF MINIMUM CORE MASSES FOR GIANT PLANET FORMATION

Ana-Maria A. Piso
Harvard-Smithsonian Center for Astrophysics

Andrew N. Youdin
JILA, University of Colorado at Boulder

Ruth A. Murray-Clay
Harvard-Smithsonian Center for Astrophysics
Draft version October 4, 2013

ABSTRACT

The core accretion model assumes that giant planets form through gas accretion on to a solid core. The core and the atmosphere initially grow simultaneously through stages of quasistatic equilibrium. Once the core becomes massive enough, the atmosphere is no longer in hydrostatic balance and a rapid phase of runaway gas accretion commences. The minimum core mass for which unstable atmosphere collapse occurs is typically called the "critical core mass". In standard calculations of the critical core mass, planetesimal accretion dominates the atmosphere evolution, and the energy deposited by incoming planetesimal on to the core is radiated away by the atmosphere. In this study we consider a low planetesimal accretion regime in which the luminosity evolution of the atmosphere is dominated by Kelvin-Helmholtz contraction. We use the atmosphere structure and cooling model developed in Piso & Youdin (2013) to derive the profile and evolution of atmospheres composed of a gas described by a realistic equation of state. We find that the minimum core mass (which we denote as *critical core mass*) to form a giant planet before the dissipation of the protoplanetary disk is substantially increased compared to an ideal gas polytrope when non-ideal effects such as hydrogen dissociation and ionization are taken into account. Moreover, our results yield lower mass cores than corresponding studies for large planetesimal accretion rates. We therefore show that it is easier to form a planet by growing the core first, then accreting a massive gaseous envelope, rather than forming the core and atmosphere simultaneously.

1. INTRODUCTION

One of the prevalent theories of giant planet formation is the core accretion model (e.g., Mizuno et al. 1978, Stevenson 1982, Bodenheimer & Pollack 1986, Wuchterl 1993, D'Angelo et al. 2011). In this model, a solid core is first formed; the core grows, and once it becomes large enough it can accumulate a massive atmosphere. In standard core accretion models, in order to form a core large enough to attract an atmosphere, a high planetesimal accretion rate is needed, on average. The atmosphere is therefore heated due to accretion of planetesimals, and as a result it radiates away energy. The envelope is in a steady state at all times, and the atmosphere mass is a function of the core mass, which implies that every core mass maps uniquely to one atmosphere mass, for a given set of disk conditions and a planetesimal accretion rate. Moreover, larger cores hold fractionally larger envelopes. As a result, the atmosphere grows faster than the core, and eventually the atmosphere mass becomes comparable to the mass of the core. At this stage, hydrostatic equilibrium breaks down and a rapid phase of runaway gas accretion commences. This core mass $M_{\rm c}$, for which the atmosphere mass $M_{\rm atm}$ satisfies $M_{\rm atm} \sim M_{\rm c}$, is called the "critical core mass" in standard studies.

However, the planetesimal accretion rate is not necessarily constant at a given location in the protoplanetary disk throughout the disk lifetime (e.g., Ikoma et al. 2000). If the planetesimal accretion rate is very low, the atmosphere can no longer gain energy due to accretion of solids, and is instead dominated by gas accretion, contracting on a Kelvin-Helmholtz timescale. In Piso & Youdin (2013; hereafter PY13) we studied the formation of giant planet atmospheres under the assumption that Kelvin-Helmoholtz gas contraction dominates the luminosity evolution of the atmosphere over planetesimal accretion. We built quasi-static two-layer atmosphere models with an inner convective region and an outer radiative region that matches smoothly onto the protoplanetary disk. We derived a cooling model to connect series of quasti-static atmospheres, and thus obtained an evolutionary history of the envelope. We defined the time t at which unstable atmosphere collapse commences as the *crossover time* $t_{\rm co}$, at which $M_{\rm atm}(t_{\rm co}) \sim M_{\rm c}$. From this we defined as *critical core mass* the minimum core mass for a protoplanet to initiate runaway gas accretion during the lifetime of the protoplanetary disk. We studied this minimum mass for a variety of disk conditions, nebular gas compositions and opacities. We found that the critical core mass decreases for larger stellocentric distances, and is smaller for lower disk temperatures and opacities and for a higher mean molecular weight of the gas.

PY13 assume that the nebular gas can be described by a polytropic equation of state (EOS) corresponding to an ideal diatomic gas: $\nabla_{\rm ad} = 2/7$. In reality, however, non-ideal effects, such as gas dissociation and ionization, have

to be taken into account. A realistic hydrogen-helium mixture can be described using tabulated equation of state tables. In this study, we use the Saumon et al. (1995) EOS tables to describe the nebular gas. We generate atmosphere profiles and estimate the atmospheric crossover time for a variety of disk conditions. From this, we determine the minimum core mass required for runaway gas accretion to commence within the typical life timescale of the protoplanetary disk. We find that the realistic equation of state yields larger critical core masses compared to the ideal gas polytrope.

This paper is organized as follows. In section 2 we review the quasi-static and evolution models derived in PY13. We discuss the variations in the adiabatic gradient, and hence in the atmosphere structure, caused by a non-ideal equation of state in section 3, and discuss the implications of this variability on the atmosphere evolution time in section 4. We determine the minimum core mass to form a giant planet during the disk lifetime when the nebular gas is described by a realistic equation of state in section 5. In section 6 we compare our results to similar results obtained in studies that consider planetesimal accretion as the dominant source of energy. Finally, we summarize our findings in section 7.

2. MODEL REVIEW

In this section we review the model developed in PY13 for the structure and evolution of a planetary atmosphere embedded in a protoplanetary disk. We describe the assumptions of the model and the properties of our assumed protoplanetary disk in section 2.1, and we summarize the equations describing the structure and time evolution of the atmosphere in section 2.2.

2.1. *Assumptions and Disk Model*

We assume that the planet consists of a solid core of fixed mass and a two-layer atmosphere composed of an inner convective zone and an outer radiative zone that matches smoothly on to the disk. The two regions are separated by the Schwarzschild criterion for convective instability. We denote the surface between the two regions as the radiative-convective boundary (RCB), defined by a radius $r = R_{\rm RCB}$. We assume a low planetesimal accretion regime in which the atmosphere evolution is dominated by KH contraction while planetesimal accretion is neglected. Moreover, we assume that the luminosity is constant throughout the outer radiative region. The atmosphere is spherically symmetric and self-gravitating. It consists of a hydrogen-helium mixture, with hydrogen and helium mass fractions of 0.7 and 0.3, respectively. We further assume that the envelope evolves through stages of quasi-static equilibrium.

The temperature and pressure at the outer boundary of the atmosphere are given by the nebular temperature and pressure. As a disk model, we use the minimum mass, passively irradiated model of Chiang & Youdin (2010). The surface density, mid-plane temperature and mid-plane pressure are given by

$$\Sigma_{\rm d} = 2200\,(a/{\rm AU})^{-3/2}\ {\rm g\ cm^{-2}} \quad (1a)$$

$$T_{\rm d} = 120\,(a/{\rm AU})^{-3/7}\ K, \quad (1b)$$

$$P_{\rm d} = 110\,(a/{\rm AU})^{-45/14}\ {\rm dyn\ cm^{-2}} \quad (1c)$$

with a the semi-major axis and for a mean molecular weight $\mu = 2.35$.

2.2. *Structure Equations and Cooling Model*

The structure of a static atmosphere is described by the standard equations of hydrostatic balance and thermal equilibrium:

$$\frac{dP}{dr} = -\frac{Gm}{r^2}\rho \quad (2a)$$

$$\frac{dm}{dr} = 4\pi r^2\rho \quad (2b)$$

$$\frac{dT}{dr} = \nabla\frac{T}{P}\frac{dP}{dr} \quad (2c)$$

$$\frac{dL}{dr} = 4\pi r^2\rho(\epsilon+\epsilon_g), \quad (2d)$$

with r the radial coordinate, P, T and ρ the gas pressure, temperature and density, respectively, m the mass enclosed by the radius r, L the luminosity from the surface of radius r. The ϵ term represents the rate at which internal heat is generated per unit mass, while $\epsilon_g \equiv -T\frac{ds}{dt}$ is the heating per unit mass due to gravitational contraction, with s the specific gas entropy. We do not take into account any internal energy sources and we therefore set $\epsilon = 0$. The expression for the temperature gradient $\nabla \equiv \frac{d\ln T}{d\ln P}$ depends on whether energy is transported throughout the atmosphere by radiation or convection. In the case of radiative diffusion for an optically thick gas, the temperature gradient is

$$\nabla = \nabla_{\rm rad} \equiv \frac{3\kappa P}{64\pi G m\sigma T^4}L, \quad (3)$$

with σ the Stefan-Boltzmann constant and κ the dust opacity. In our models the atmosphere is optically thick throughout the outer boundary. On the other hand, when the energy is transported outwards through convection, the temperature gradient is given by

$$\nabla = \nabla_{\rm ad} \equiv \Big(\frac{d\ln T}{d\ln P}\Big)_{\rm ad}, \quad (4)$$

with $\nabla_{\rm ad}$ the adiabatic temperature gradient. The convective and radiative layers of the envelope are separated by the Schwarzschild criterion (e.g., Thompson 2006): the atmosphere is stable against convection when $\nabla < \nabla_{\rm ad}$ and convectively unstable when $\nabla > \nabla_{\rm ad}$. For effective convection, $\nabla \approx \nabla_{\rm ad}$. The temperature gradient is thus given by $\nabla = \min(\nabla_{\rm ad}, \nabla_{\rm rad})$.

The equation set (2) is supplemented by an equation of state (EOS) relating pressure, temperature and density, as well as an opacity law. In this study we use the interpolated EOS tables of Saumon et al. (1995) for a helium mass fraction $Y = 0.3$. More details on the EOS tables and the methodology of combining the separate tables for hydrogen and helium are presented in section 3 and Appendix A.

We assume a standard ISM opacity power law given by

$$\kappa = \kappa_0\Big(\frac{P}{P_{\rm ref}}\Big)^{\alpha}\Big(\frac{T}{T_{\rm ref}}\Big)^{\beta}, \quad (5)$$

with α, β, κ_0 constants, and $T_{\rm ref}$ and $P_{\rm ref}$ a normalizing temperature and pressure, respectively. To estimate α, β and κ_0 we use the Bell & Lin (1994) opacity laws for ice grains: $\alpha = 0$, $\beta = 2$ and $\kappa_0 = 2$. These values are valid only for low disk temperatures: $T_d \lesssim 100K$. We therefore consider protoplanets that form in the outer parts of the disk where temperatures are low, i.e. $a \geq 5$ AU. Dust settling or grain growth will result in different numerical values for the κ_0 and β coefficients.

We further discuss our choice of core parameters and boundary conditions. We assume a solid core of fixed mass $M_{\rm c}$ with a radius $R_{\rm c} = (3M_{\rm c}/4\pi\rho_{\rm c})^{1/3}$, where $\rho_{\rm c}$ is the core density. We choose $\rho_{\rm c} = 3.2$ g cm^{-3} (e.g., Papaloizou & Terquem 1999). The atmosphere is assumed to match on to the protoplanetary at the Hill radius, $R_{\rm H} \equiv a\left(\frac{M_{\rm p}}{3M_\odot}\right)^{1/3}$, the distance at which the gravitational attraction of the planet and the tidal gravity due to the host star are equal. Outside the Hill sphere, the gravity of the planet is overcome by the tidal gravity from its host star, and hence only gas that lies within the Hill sphere can be gravitationally bound to the planet. The effective outer boundary of the atmosphere is the surface defined by the Bondi radius, $R_{\rm B} \equiv \frac{GM_{\rm p}}{c_{\rm s}^2} = \frac{GM_{\rm p}}{\mathcal{R}T_{\rm d}}$. This is the distance from the planet at which the thermal energy of the nebular gas is of the order of the gravitational energy of the planet. Here G is the gravitational constant, $M_{\rm p}$ is the total mass of the planet, $c_{\rm s}$ is the isothermal sound speed, and $\mathcal{R}$ is the reduced gas constant: $\mathcal{R} = k_b/(\mu m_p)$, with k_b the Boltzmann constant and m_p the proton mass. Outside the Bondi sphere, the gravity of the planet is too weak to significantly affect the nebular gas, which justifies the choice of Bondi radius as the relevant radius of the atmosphere. However, the nebular gas is still perturbed outside the Bondi sphere, and therefore the Hill radius is the correct scale for matching on to the disk. This choice for the atmosphere boundary applies only when the Bondi radius is smaller than the Hill radius; when $R_{\rm B} > R_{\rm H}$, the atmosphere only extends out to the Hill radius, since material cannot be gravitationally bound to the protoplanet outside the Hill sphere. At the Hill radius, the temperature and pressure are given by the nebular temperature and pressure: $T(R_{\rm H}) = T_{\rm d}$ and $P(R_{\rm H}) = P_{\rm d}$. For a given core mass, the atmosphere profile and evolution are therefore uniquely determined by the outer boundary conditions.

Lastly, we review the cooling model developed in PY13 used to determine the time evolution of the atmosphere between subsequent static models. A protoplanetary atmosphere embedded in a gas disk satisfies the following cooling equation:

$$L = L_c + \Gamma - \dot{E} + e_{\rm acc}\dot{M} - P_M\frac{\partial V_M}{\partial t} \qquad (6)$$

Here, L is the total luminosity, $L_{\rm c}$ is the luminosity from the solid core, and may include planetesimal accretion and radioactive decay, Γ is the rate of internal heat generation, $\dot{E}$ is the rate at which total energy (internal and gravitational) is lost, and $e_{\rm acc}$ is the specific total energy brought in by mass accreting at the rate $\dot{M}$: $e_{\rm acc} = u - GM/R$. The last term represents the work done on a surface mass element.

We obtain an evolutionary series for the atmosphere by connecting sets of subsequent static atmospheres through the cooling equation (6). Details of our numerical procedure are described in PY13.

3. ADIABATIC GRADIENT FOR THE TABULATED EQUATION OF STATE

This section explains how non-ideal EOS effects influence the behavior of the thermodynamic variables when compared to an ideal gas polytrope. Figure 1 shows a contour plot of the adiabatic gradient (defined in equation 4) as a function of gas temperature and pressure, which was obtained by interpolating and extending the Saumon et al. (1995) EOS tables as described in Appendix A.

We distinguish three separate temperature regimes:

1. Intermediate temperature regime (300 K $\lesssim T \lesssim$ 3000 K), where the hydrogen-helium mixture behaves like an ideal gas with a polytropic EOS.
2. High temperature regime ($T \gtrsim$ 3000 K), where dissociation of molecular hydrogen occurs, followed by ionization of atomic hydrogen.
3. Low temperature regime ($T \lesssim$ 300 K), where the rotational states of the hydrogen molecule are not fully excited.

We note that helium behaves like an ideal monatomic gas with $\nabla_{\rm ad} = 2/5$ in our regime of interest. Its presence in the atmosphere thus only causes a small, constant upper shift in the adiabatic gradient of the mixture.

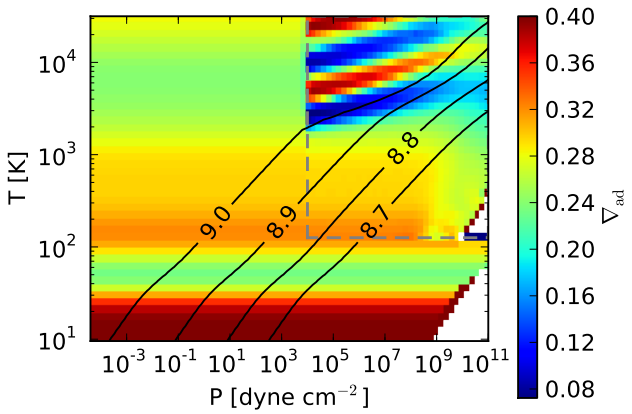

FIG. 1.— Contour plot of the adiabatic gradient $\nabla_{\rm ad}$ for a hydrogen-helium mixture as a function of gas temperature and pressure. The upper right rectangle encloses the region described by the original Saumon et al. (1995) EOS tables, while the rest of the plot is our extension to lower temperatures and pressures. The black curves represent constant entropy adiabats, with the labels the natural logarithm of the absolute entropy per unit mass. At high temperatures, hydrogen dissociates and ionizes, while at low temperatures the rotational states of the hydrogen molecule are only partially excited and it no longer behaves like an ideal diatomic gas. Our extension matches smoothly with the original tables in our regime of interest (encompassed by the constant entropy curves).

In what follows we explain the behavior of the adiabatic gradient in the three temperature regimes separately.

1. Intermediate T: Ideal Gas

For temperatures less than ~ 2000 K but larger than ~ 300 K, the hydrogen molecule is not energetic enough to dissociate and hydrogen behaves as an ideal diatomic gas. We see this in Fig. 1 for 300 K $\lesssim T \lesssim$ 3000 K, where the adiabatic gradient is approximately constant. The helium component of the gas causes a slight increase in the adiabatic index: $\nabla_{\rm ad} \approx 0.3$ in this temperature range rather than 2/7 as is the case for a diatomic gas.

2. High T: Dissociation and Ionization of Hydrogen.

At low temperatures, hydrogen exists in molecular form and has a stable configuration. As the temperature becomes higher than $T \sim 2000 - 3000$ K, the internal energy of the hydrogen molecule becomes large enough to break the covalent bond between the atoms, and hydrogen starts dissociating. Further energy increase at temperatures of $\sim 10^4$ K results in electrons being removed from atoms, i.e. hydrogen ionizes. In stellar and giant planet interiors there is little overlap between the two processes: hydrogen is almost entirely dissociated into atoms by the time ionization becomes important.

We see in Figure 1 that the adiabatic gradient decreases significantly in regions of partial dissociation and partial ionization. This behavior is different than that of a mixture of molecular and atomic hydrogen (a mixture of protons and electrons), where $2/7 < \nabla_{\rm ad} < 2/5$ ($\nabla_{\rm ad} = 2/5$). We explain this in what follows.

For a mixture of ideal gases, the total internal energy is given by the sum of the internal energies of the individual gases. When a gas dissociates, however, the energy used to break down the molecules has to also be taken into account. This energy depends on the dissociation fraction and can be determined from the Saha equation (see e.g., Kippenhahn & Weigert 1990). The dissociation fraction only depends on gas temperature and density (see Appendix B), and hence only on the EOS. An expression for the adiabatic gradient as a function of the dissociation fraction is presented in Appendix B. As expected, the adiabatic gradient is $\nabla_{\rm ad} = 2/7$ for pure molecular hydrogen and $\nabla_{\rm ad} = 2/5$ when hydrogen is fully dissociated, but decreases significantly during partial dissociation and it is smallest when half of the gas is dissociated.

This is consistent with the behavior we see in Figure 1. At constant entropy, an increase in pressure results in an increase in the internal energy of the system, which usually causes the temperature to rise significantly. During partial dissociation, however, part of the internal energy is used to remove the electrons from atoms, and therefore there is less energy available to increase the temperature of the system. This behavior of constant entropy curves is seen in Figure 1.

The ionization of atomic hydrogen is also dictated by the Saha equation, with the dissociation energy replaced by ionization energy (equal to 13.6 eV for hydrogen, e.g. Mandl 1989), hence the adiabatic gradient has an analogous behavior, consistent with Fig. 1.

3. Low T: Hydrogen Rotation and Spin Isomers

As a diatomic molecule, hydrogen has five degrees of freedom, three associated with translational motion and two associated with rotation. At room temperature, the rotational states are fully excited. The excitation temperature for rotation is $\Theta_r \approx 85$ K for the hydrogen molecule (e.g., Kittel et al. 1981); as the gas temperature becomes comparable to Θ_r, fewer rotational states are excited and rotation entirely ceases as $T \to 0$.

Molecular hydrogen occurs in two isomeric forms: orthohydrogen, with parallel proton spins, and parahydrogen, with antiparallel proton spins. The Pauli exclusion principle requires the total wavefunction of two fermions, such as protons, to be antisymmetric. As such, a symmetric spin wavefunction requires an antisymmetric rotational wavefunction, and vice-versa (Farkas 1935). Parahydrogen has an antisymmetric spin wavefunction, which means that it can only occupy symmetric rotational states and hence the angular quantum number j has to be even. By analogy, orthohydrogen must have an antisymmetric rotational wavefunction and can only occupy states with odd j. The partition functions for ortho- and parahydrogen are described in Appendix A. At equilibrium, the relative abundance of the ortho and para states is given by the ratio of their partition functions. For very low temperatures there is only parahydrogen, as molecules are in the ground state with $j = 0$, which corresponds to the para state. As the temperature is increased, parahydrogen starts converting into orthohydrogen, resulting in an ortho-para equilibrium ratio of 3:1 at room temperature.

The internal energy and specific heat per unit mass associated with rotation for the individual isomers and for the equilibrium mixture can be derived from equations (A5), (A6), (A7), (A11) and (A13) and plotted in Figure 2 (see also Farkas 1935, Figure 1). The para state has no rotational energy for low temperatures, since all the molecules occupy the rotational level with $j = 0$. Orthohydrogen, on the other hand, is in the $j = 1$ state, and so has an energy given by the energy of its first rotational level. Since all the hydrogen mixtures behave like monatomic gases at low temperatures, their rotational heat capacity is zero in this region. This is consistent with $\nabla_{\rm ad} = 2/5$ at low temperatures as seen in Fig. 1. There are two significant maxima in the heat capacities of parahydrogen and of the mixture. At very low temperatures, the heat capacity of parahydrogen is zero because only the lowest accessible energy level $j = 0$ is occupied and a temperature increase does not provide enough energy to populate the next higher level. When the temperature becomes sufficiently high to populate the second lowest level $j = 2$, the heat capacity rapidly increases, passes through a maximum and starts to decrease when the second lowest level becomes saturated. The maxima in the ortho-para mixture appears around the time when parahydrogen starts converting into orthohydrogen. The heat capacity of the equilibrium mixture is not a weighted average of the heat capacities of the individual components because it takes into account both the rotational energy uptake of para- and ortho-hydrogen, and also the shift in their equilibrium concentrations with temperature. At $T = 0$, only para-hydrogen is present in the equilibrium mixture; as the temperature is increased, the energetically higher-lying ($j = 1$) ortho-hydrogen is formed, and the concomitant energy increase is seen as a peak in the heat capacity. As the adiabatic gradient is inversely proportional to the heat capacity, it means that the former has to first decrease from 2/5 as the

temperature increases, reach a minimum around 50 K ($\nabla_{\rm ad} \approx 0.25$ from Fig. 1), then gradually increase to 2/7 as for a diatomic gas. This behavior is illustrated in Fig. 1.

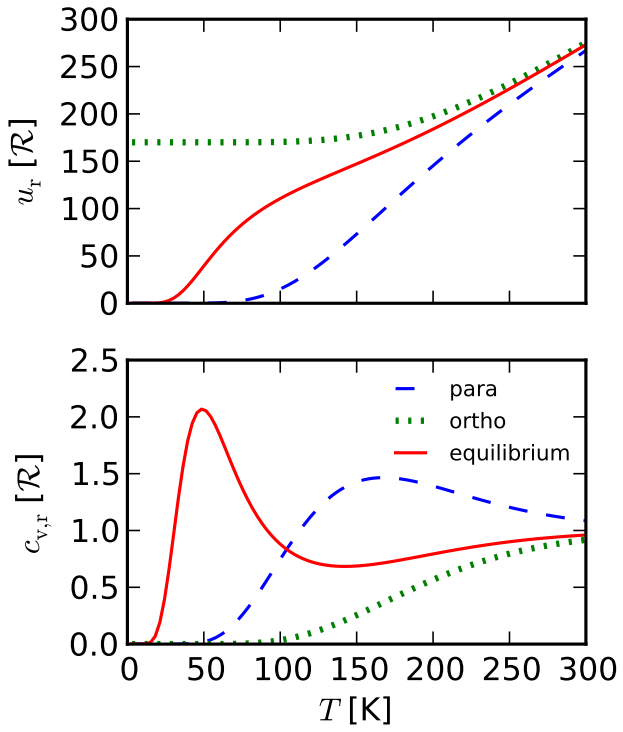

FIG. 2.— Internal energy and heat capacity per unit mass for the hydrogen spins isomers and the equilibrium mixture as a function of temperature. See Farkas (1935), Figure 1, for a similar plot.

4. EQUATION OF STATE EFFECTS ON ATMOSPHERE EVOLUTION

Variations in the adiabatic gradient $\nabla_{\rm ad}$ have two competing effects on the atmosphere evolution: they yield a lower envelope luminosity when compared to an ideal gas, and a larger amount of energy that needs to be radiated per unit mass, which slows down accretion. Together, they result in changes in the growth time of the atmosphere, and therefore in the crossover time and critical core mass (both defined in section 1). We explore the effect of partial dissociation and hydrogen spin isomers (see section 3) on the atmosphere luminosity and cooling time evolution. Due to the equation of state described in section 3, a realistic atmosphere will not have a constant adiabatic gradient $\nabla_{\rm ad}$, as was assumed in PY13. We thus first investigate the differences in atmosphere profiles and evolution for ideal gas polytropes with different adiabatic gradients in section 4.1. We then show how the variable adiabatic gradient affects the time evolution of the atmosphere in section 4.2.

4.1. *Ideal Gas Polytropes with Different Adiabatic Gradient*

In this section we investigate the differences in luminosity and dE/dM, and the resulting time evolution, between ideal gas polytropes with different adiabatic gradients: $\nabla_{\rm ad} = 2/7$ (diatomic gas) and $\nabla_{\rm ad} = 2/5$ (monatomic gas). We assume both gases have the same mean molecular weight.

We generate atmosphere profiles for the two different adiabatic indices at $a = 10$ AU and for a core mass $M_{\rm c} = 10 M_\oplus$, and estimate the luminosity and cooling time evolution as described in section 2. The results are shown in Figure 3. We find that the polytrope with the lower adiabatic gradient has both a higher luminosity and a longer cooling time. We use instantaneous atmosphere profiles to explain these effects.

Figure 4, top panel, shows the temperature profile for the two polytropes at a fixed total mass $M_{\rm tot} = 15 M_\oplus$. The polytrope with a larger adiabatic gradient, $\nabla_{\rm ad} = 2/5$, has a more shallow convective zone, and hence a deeper radiative region, since a larger temperature gradient delays the onset of convection. A deeper radiative layer increases the number of steps that photons need to diffuse, resulting in a lower luminosity as seen in the top panel of Figure 3.

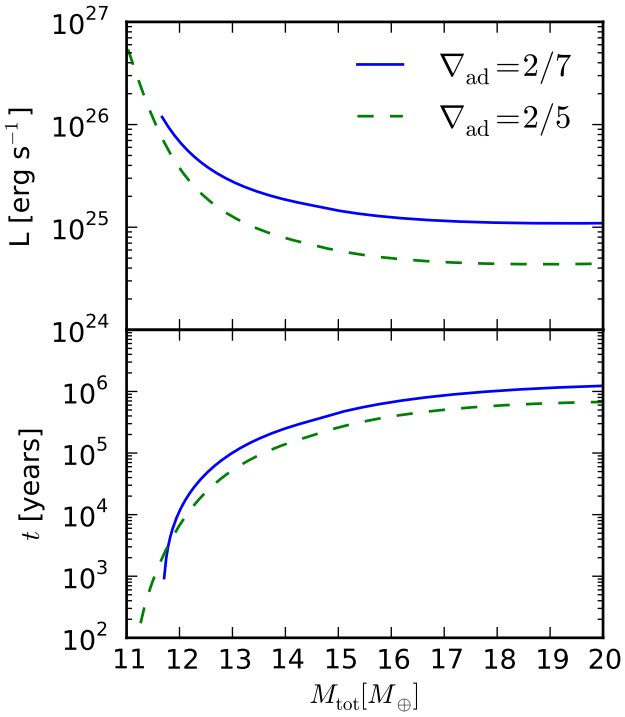

FIG. 3.— Luminosity and time evolution as a function of total mass (core + atmosphere) for polytropes with different adiabatic indices, for a planet forming at 10 AU and with a fixed core mass $M_{\rm c} = 10 M_\oplus$. A larger adiabatic index results in both a lower luminosity and a shorter cooling time.

The bottom panel of Figure 4 shows an instantaneous energy profile for the same total mass $M_{\rm tot} = 15 M_\oplus$. The bulk of the energy is concentrated deep in the atmosphere for the $\nabla_{\rm ad} = 2/7$ polytrope and towards the outer boundary for the $\nabla_{\rm ad} = 2/5$ polytrope. Qualitatively, this can be explained through a simple analytic argument: the density profile in an adiabatic, non-self gravitating atmosphere composed of an ideal gas scales

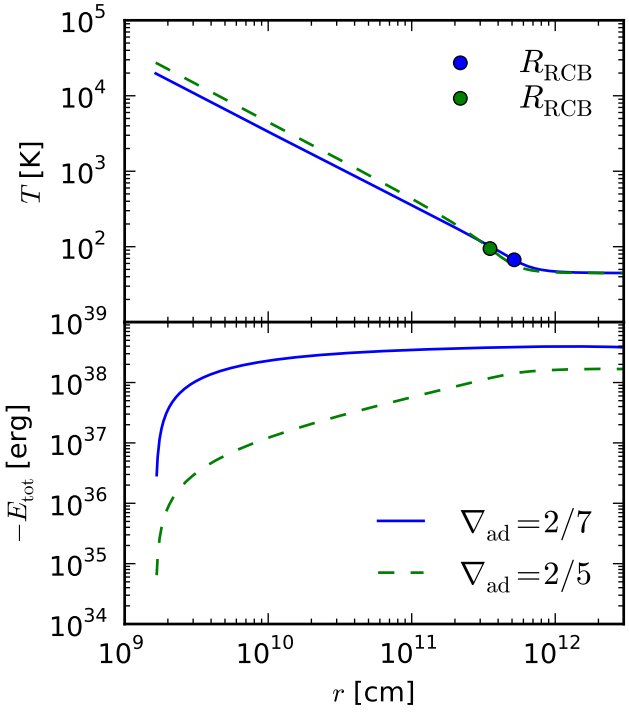

FIG. 4.— Instantaneous temperature and total energy profiles as a function of radius for polytropes with different adiabatic indices, for a planet forming at 10 AU and with a fixed core mass $M_{\rm c} = 10M_{\oplus}$. The total mass (core + atmosphere) is $15M_{\oplus}$. The location of the radiative-convective boundary is marked. A lower adiabatic gradient results in a more shallow radiative region (upper panel), and in the total energy being concentrated at the bottom of the atmosphere (lower panel).

as $\rho(r) \sim r^{1/(\gamma-1)}$ with γ the adiabatic index (see PY13). Since the energy per unit mass scales as $e(r) \sim \rho(r)r^2$, we find that only polytropes with $\gamma < 3/2$, i.e. $\nabla_{\rm ad} < 1/3$, have the total energy concentrated towards the core. This is satisfied by $\nabla_{\rm ad} = 2/7$ but not by $\nabla_{\rm ad} = 2/5$, in agreement with the results in the bottom panel of Figure 4. It takes more energy to bring in gas deep in the atmosphere for an envelope that has the bulk of its energy concentrated towards the bottom, which increases $|dE/dM|$ for the $\nabla_{\rm ad} = 2/7$ polytrope.

We find that the energy effect prevails over the luminosity effect, resulting in a longer cooling time for the polytrope with the lower adiabatic gradient (i.e., $\nabla_{\rm ad} = 2/7$), as shown in the bottom panel of Figure 3.

4.2. *Dissociation and Spin Isomers Effects*

In this section we use the results obtained in section 4.1 to explain the effects on the atmosphere evolution of a realistic equation of state. We explore the effect of hydrogen dissociation at the high temperatures in the inner part of the atmosphere, and the effect of hydrogen spin isomers at the low temperatures at the top of the atmosphere separately. In order to do this, we generate atmosphere profiles in which the nebular gas is assumed to be described by a combination of ideal and realistic equations of state, depending on the temperature. To explain the effects of the hydrogen spin isomers in the outer parts of the atmosphere, we assume that the realistic EOS effects only matter at low temperatures; conversely, we assume that the realistic EOS effects are important only at high temperatures in order to study the effects of hydrogen dissociation deep in the atmosphere. As such, we generate three sets of atmosphere profiles, choosing $a = 10$ AU and $M_{\rm c} = 5M_{\oplus}$. The first one is described by a realistic EOS for temperatures larger than 500 K and by an ideal gas with $\nabla_{\rm ad} = 0.3$ for $T < 500$ K. The second profile consists of an ideal gas polytrope with $\nabla_{\rm ad} = 0.3$ for $T > 500$ K and a realistic gas in the low temperature regime. Finally, the last profile corresponds to an ideal gas with $\nabla_{\rm ad} = 0.3$, the adiabatic gradient of an ideal hydrogen-helium mixture. We choose $T = 500$ K as the reference temperature since the adiabatic gradient of the realistic gas is roughly constant around this temperature (see Figure 1). The differences in atmosphere structure and evolution between the ideal gas and the realistic gas at low (high) temperatures highlight the effects of hydrogen spin isomers (hydrogen dissociation). Figure 5 illustrates the differences in time evolution between these profiles. We see that both dissociation and spin isomers have a comparable effect on the atmosphere growth, and result in slower cooling, and therefore a longer crossover time, when compared to the polytropic ideal gas equation of state. The cooling time is dependent on both the total energy released due to the contraction of the envelope and the luminosity of the atmosphere. In what follows we explore the relative influence of these two factors separately.

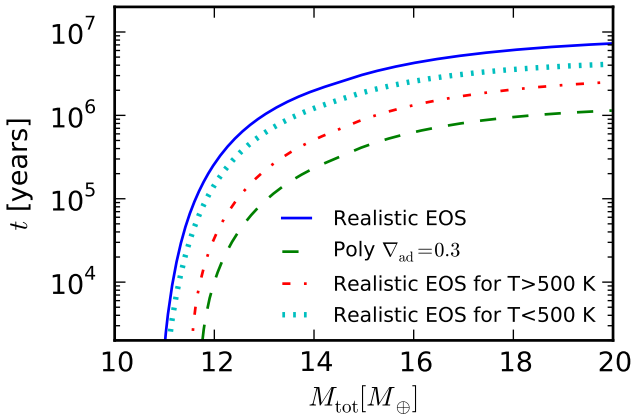

FIG. 5.— Cooling time evolution as a function of total mass (core + atmosphere) for a variety of EOS combinations, for a planet forming at 10 AU and with a fixed core mass $M_{\rm c} = 10M_{\oplus}$. The cooling time is larger for the realistic EOS both due to hydrogen dissociation and spin effects when compared to an ideal gas polytrope.

The right panel of Figure 6 shows the luminosity evolution with mass for the three combinations of equations of state described above, as well as for the complete realistic gas EOS. Similarly to section 4.1, we use instantaneous atmosphere profiles to explain the differences. The left panel of Figure 6 shows the instantaneous temperature profile and the location of the radiative-convective boundary for a total fixed mass (core + atmosphere) $M_{\rm tot} = 11.8M_{\oplus}$. The realistic equation of state for low

temperatures is characterized by a lower adiabatic index in the outer regions, due to the spin effects, and is therefore dominant in the radiative zone. As a result, it generates a deeper radiative zone with a lower luminosity, which explains the results in the left panel of Figure 6. Moreover, since the cooling time is inversely proportional to the luminosity, the spin effect will result in a longer cooling time.

The energy behavior is shown in Figure 7. The realistic EOS for high temperatures has a low adiabatic index deep in the atmosphere, due to hydrogen dissociation, and thus the bulk of its energy concentrated at the bottom of the atmosphere, for the reasons described in section 4.1. It takes more energy to add mass more mass deep in the atmosphere, and $|dE/dM|$ is larger as a result.

We have seen that the spin effect at the outer boundary dictates the location of the radiative zone, and therefore the luminosity behavior, while dissociation deep in the atmosphere dictates the energy behavior. Overall, both effects result in a longer time for the atmosphere to evolve.

5. CRITICAL CORE MASS

In this section we put together the results obtained in section 4 and determine the minimum core mass to initiate runaway gas accretion during the lifetime of the protoplanetary disk assuming that the nebular gas is described by a realistic equation of state as prescribed by the Saumon et al. (1995) EOS tables (see section 4). As in PY13, we define this minimum core mass as the *critical core mass*. Moreover, we define the time elapsed until runaway gas accretion is initiated when $M_{\rm atm} \sim M_{\rm c}$ as the *crossover time*. In this section we first explore the dependence of the crossover time on the core mass for a fixed semi-major axis. We then determine the critical core mass to form a giant planet before the dissipation of the gas in the protoplanetary disk, assuming that the nebular gas is described by a realistic hydrogen-helium mixture, and we compare this with the results from PY13 for an ideal diatomic gas. Finally, we determine the critical core mass under more realistic opacity assumptions.

Figure 8 displays the time evolution and the crossover time for core masses between 7 and 16 $M_\oplus$ at $a = 10$ AU in our fiducial disk. The crossover time is shorter for higher mass cores, consistent with the results of PY13.

Figure 9 shows the critical core mass for a massive atmosphere to form during a typical lifetime of a protoplanetary disk $t = 3$ Myrs, for a gas described by a realistic equation of state. For comparison, we also plot the results of PY13 for an ideal diatomic gas. The use of a realistic equation of state increases the critical core mass by more than a factor of 2. As such, non-ideal effects substantially affect the core mass needed to form a giant planet before the dissipation of the protoplanetary disk.

The above results were obtained under the assumption that the dust opacity in the radiative region of the atmosphere is given by the standard ISM opacity (see also section 2.2). However, our scenario of low planetesimal accretion is likely to favor lower dust opacities, due to grain growth and dust settling. Grain growth, in particular, lowers the absolute value of the opacity and changes the particle size distribution when compared to the standard ISM size distribution (e.g., Pollack et al. 1985).

Although grain growth has been observed in protoplanetary disks (e.g., Beckwith et al. 1990, Beckwith & Sargent 1991, Pérez et al. 2012), the size distribution of dust particles has not been observationally constrained. Typically, the grain size distribution is assumed to be a power law:

$$n \sim a^{-p}, \tag{7}$$

where a is the particle radius and $p = 3.5$ (corresponding to a "normal" collisional cascade) or $p = 2.5$ (an approximation for coagulation). In this work we use the D'Alessio et al. (2001) frequency-dependent opacity tables to obtain the temperature-dependent Rosseland mean opacity κ, assuming a maximum particle size of 1 cm and a grain size distribution given by equation (7) with $p = 3.5$.

The D'Alessio et al. (2001) opacities are only relevant at temperatures that are sufficiently low for dust grains to remain solid ($T \lesssim 1000$ K). In the temperature regime where dust sublimates we use the Bell & Lin (1994) analytic opacity laws, ensuring smooth transition from the grain growth opacities.

The sharp drop in opacity ($\kappa \sim T^{-24}$) due to dust sublimation lowers the radiative temperature gradient significantly (see equation 3), and may therefore generate radiative layers within the inner region of the atmosphere (see Appendix C, Figure 17). This can potentially pose challenges for our model, since the additional luminosity generated in these radiative windows may be large enough to make our assumption of constant luminosity throughout the radiative layers invalid. However, the inner radiative windows are either very thin (Figure 17, middle panel), or the temperature gradient is flat enough to result in a roughly constant luminosity throughout the region (Figure 17, bottom panel; also see equation 2c). This results in a negligible extra luminosity generated in the radiative windows.

Despite the existence of one or more radiative windows in the planet atmosphere, the luminosity that emerges at the outer boundary is set by the top radiative window, as is the case for the standard inner convective-outer radiative envelopes. The equation of radiative diffusion (2c) can be approximated in terms of the radiative flux $\mathcal{F}$ as

$$\mathcal{F} \sim \frac{\sigma T_{\rm RCB}^4}{\tau}, \tag{8}$$

where τ is the optical depth of the upper radiative layer. Furthermore, we find that τ is dominated by the optical depth of the first scale height, i.e.

$$\tau \sim \tau_{\rm RCB} = \kappa_{\rm RCB}\rho_{\rm RCB}H_{\rm RCB}, \tag{9}$$

where

$$H_{\rm RCB} = \frac{k_b T_{\rm RCB}}{\mu m_H}\frac{R_{\rm RCB}^2}{GM_{\rm RCB}}, \tag{10}$$

with k_b the Boltzmann constant, μ the mean molecular weight of the gas, m_H the proton mass, and all other quantities evaluated at the bottom of the radiative layer. By substituting equations (10) and (9) into equation (8), and noting that $\mathcal{F} = L/(4\pi(R_{\rm RCB} + H_{\rm RCB})^2) \approx L/(4\pi R_{\rm RCB}^2)$, we recover equation (3) applied at the

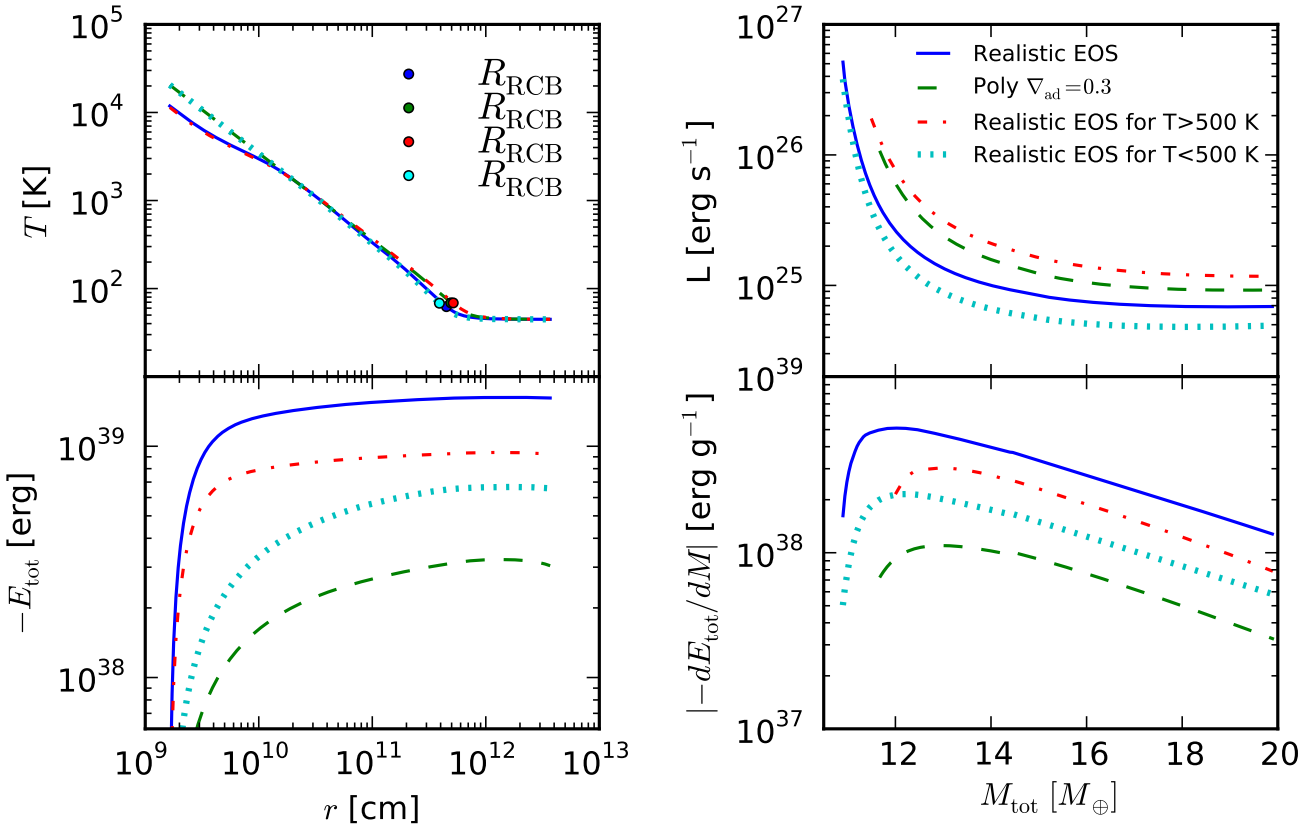

FIG. 6.— Left panel: Instantaneous temperature profile as a function of radius for a variety of EOS combinations, for a planet forming at 10 AU and with a fixed core mass $M_{\rm c} = 10M_\oplus$. The total mass (core + atmosphere) is $11.8M_\oplus$. The location of the radiative-convective boundary is marked. The effect of hydrogen spin isomers at low temperatures in the outer region of the atmosphere sets the location of the radiative-convective boundary. Right panel: Luminosity evolution as a function of total mass (core + atmosphere) for a variety of EOS combinations, for a planet forming at 10 AU and with a fixed core mass $M_{\rm c} = 5M_\oplus$. The existence of the hydrogen spin isomers at low temperatures near the top of the atmosphere results in a lower luminosity. The two effects combined yield a lower luminosity for the realistic equation of state when compared to the polytrope.

boundary between the uppermost convective region of the atmosphere and the outer radiative layer (where $\nabla_{\rm rad} = \nabla_{\rm ad}$).

Due to the variable number and position within the planet atmosphere of radiative windows, and therefore of radiative-convective boundaries, we cannot calculate the time evolution of different atmospheres if we evaluate our cooling equation (6) at the RCB, as we do in our standard model. We choose to evaluate the cooling time at the Bondi radius instead (since our cooling model applies at any radius R, see section 2.2). We note that our choice of R does not change the estimate of the atmosphere evolution time, to order of magnitude, since the additional luminosity generated in all radiative regions is negligible (see PY13).

Figure 10 shows the resulting critical core mass as a function of semi-major axis. The critical core mass is lower than in the standard case, and less sensitive to the distance in the disk, i.e. the boundary conditions (temperature and pressure). We have shown in PY13 that the critical core mass is highly dependent on disk temperature rather than pressure. The temperature dependence, however, is mainly due to opacity: for the simplified analytic model developed in PY13 we found that the crossover time $t_{\rm co} \sim T^{\beta+1/2}$, with β the power-law exponent in equation (5). Opacity is less sensitive to temperature variations for larger grains and has an almost flat profile (see Figure 18), which results in $\beta \ll 1$ and a much weaker temperature (and therefore semi-major axis) dependence of the critical core mass, as seen in Figure 10. Moreover, grain growth reduces the absolute value of the opacity, which results in an overall lower crossover time and critical core mass.

In our calculation so far we assumed that the size distribution of dust grains is the power law (7) with $p = 3.5$, which corresponds to a normal collisional cascade. If, however, coagulation is taken into account, the exponent p can be approximated as $p = 2.5$ (D'Alessio et al. 2001). This results in a flatter and significantly lower opacity, which may substantially reduce the critical core mass. However, we have found that our model breaks down for low core masses ($M_{\rm c} \lesssim 3M_\oplus$) under this assumption, i.e. the outer radiative region becomes deep enough that the luminosity generated in this region can no longer be neglected. Figure 11 shows the crossover time as a function of semi-major axis for the lowest core mass in which our model is valid, $M_{\rm c} = 4M_\oplus$. The crossover time is more than one order of magnitude lower when coagula-

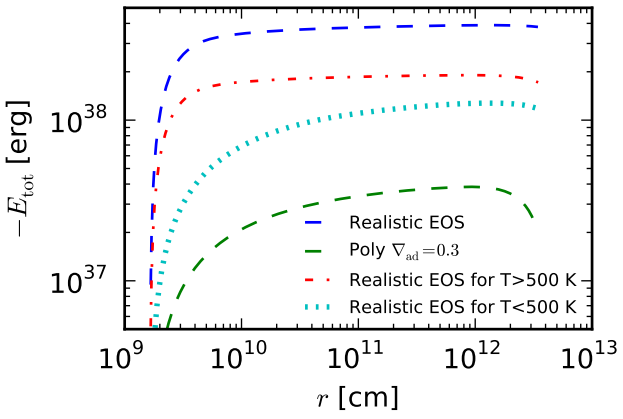

FIG. 7.— Instantaneous energy profiles as a function on radius for a variety of EOS combinations, for a planet forming at 10 AU and with a fixed core mass $M_{\rm c} = 10M_{\oplus}$. The total mass (core + atmosphere) is $11.8M_{\oplus}$. Hydrogen dissociation deep in the atmospheres causes the bulk of the energy to be concentrated at the bottom of the atmosphere. This increases the amount of energy per unit mass that needs to be radiated away, i.e. $|dE/dM|$, resulting in a longer crossover time for the realistic EOS when compared to the polytrope.

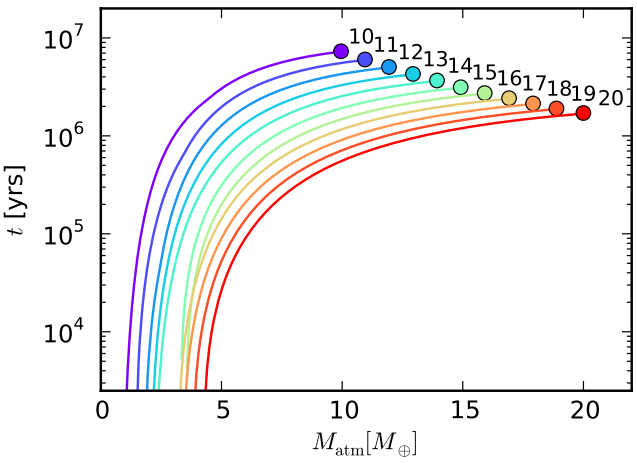

FIG. 8.— Time to grow an atmosphere of mass $M_{\rm atm}$ for cores with fixed masses between $10M_{\oplus}$ and $20M_{\oplus}$ at $a = 10$ AU in our fiducial disk. The circles mark the crossover time where $M_{\rm atm} \sim M_{\rm c}$. The numbers are labeling the core mass in Earth masses. A larger core mass results in a shorter crossover time.

tion is accounted for, which implies that the critical core mass may be, in fact, significantly lower than presented in Figure 10.

6. EFFECTS OF PLANETESIMAL ACCRETION

In this study we have considered atmospheres for which planetesimal accretion is negligible and Kelvin-Helmholtz contraction dominates the luminosity evolution of the atmosphere. This is different from standard analytic calculations, in which the atmosphere is heated by planetesimal accretion. In this section we compare our results for the critical core mass to analogous results from the analytic calculations. We discuss the core accretion rates that are necessary for our regime to be valid

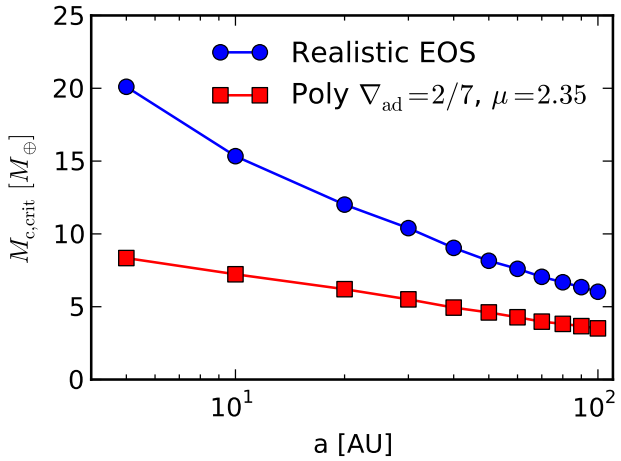

FIG. 9.— The minimum core mass for an atmosphere to initiate runaway gas accretion within the lifetime of a typical protoplanetary disk $t \sim 3$ Myrs as a function of semi-major axis, for a realistic hydrogen-helium mixture. The results of PY13 for an ideal diatomic gas are plotted for comparison. The realistic equation of state yields core masses larger by more than a factor of 2 when compared to the polytrope.

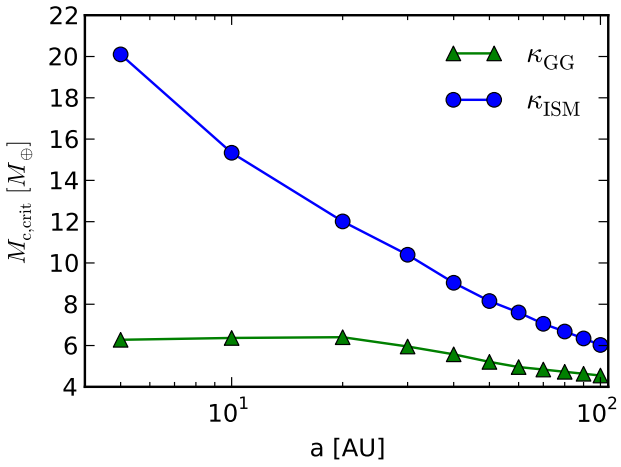

FIG. 10.— Critical core mass as a function of semi-major axis for grain growth opacity.

in section 6.1. We then compare our results with planetesimal accretion results under similar assumptions in section 6.2.

6.1. *Planetesimal Accretion Rates*

We estimate the planetesimal accretion rate consistent with our assumptions that $L_{\rm acc} \ll L_{\rm KH}$. Here $L_{\rm acc}$ is the accretion luminosity given by

$$L_{acc} = G\frac{M_{\rm c}\dot{M}_{\rm c}}{R_{\rm c}}, \qquad (11)$$

where $\dot{M}_{\rm c}$ is the planetesimal accretion rate, and $L_{\rm KH}$ is the luminosity of the atmosphere due to gas contraction obtained from our static model described in section 2. At the limit, $L_{\rm acc} = L_{\rm KH}$. For a given atmosphere model we can therefore estimate the maximum planetesimal accre-

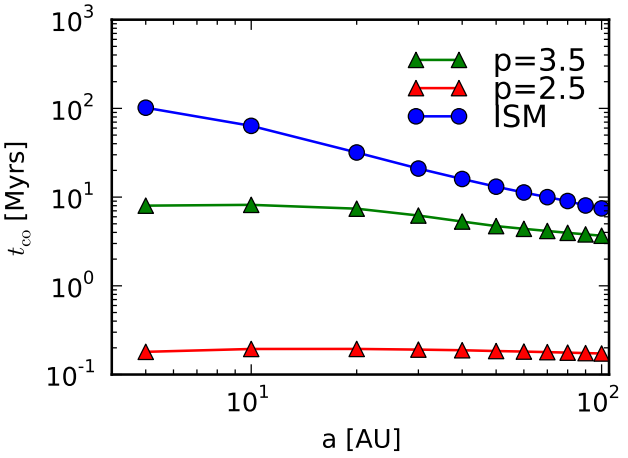

FIG. 11.— Crossover time for different grain size distribution.

tion rate during the contraction of the envelope in order for the atmosphere to be dominated by gas contraction. We choose as a fiducial case an atmosphere forming at 60 AU and with a core mass of $5M_\oplus$. Since analytic studies assume an ideal gas EOS, our fiducial atmosphere is described by an ideal gas polytrope with constant adiabatic gradient $\nabla_{ad} = 2/7$ and mean molecular weight $\mu = 2.35$ (see also PY13). For this choice of parameters, the atmosphere crossover time is $t_{co} \sim 2.1$ Myrs, which is within the typical life time of a protoplanetary disk. The results are presented in Figure 12.

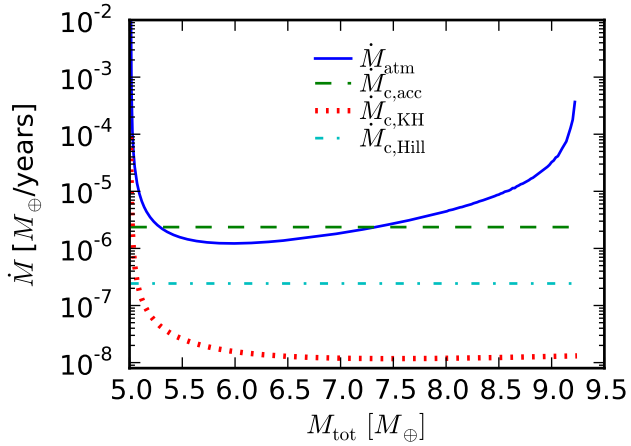

FIG. 12.— Various relevant accretion rates in the case of a planet forming at 60 AU and with a core mass $M_c = 5M_\oplus$. The $\dot{M}_{atm}$ curve represents the growth rate of the atmosphere as estimated by our model, and $\dot{M}_{c,KH}$ is the maximum planetesimal accretion rate during the gas contraction phase in order for our regime to be valid. For comparison, we plot the core accretion rate $\dot{M}_{c,acc}$ necessary to grow the core on the same time scale as the atmosphere $\tau \sim 2.1$ Myrs, and a typically assumed planetesimal accretion rate $\dot{M}_{c,Hill}$ where the random velocity of the planetesimals is given by the Hill velocity due to the core.

We label the resulting minimum core accretion rate as $\dot{M}_{c,KH}$, with $\dot{M}_{c,KH} = \frac{L_{KH}R_c}{GM_c}$ from equation (11). The atmosphere growth rate $\dot{M}_{atm}$ is also plotted for comparison. We see that the core accretion rate has to be $\sim 2-3$ orders of magnitude lower than the atmosphere accretion rate for our assumptions to be valid. If the core had accreted planetesimals at this constant rate since it started forming, then the formation of a core massive enough to attract an atmosphere would not have been possible within a typical disk lifetime, implying that planetesimal accretion must have been larger initially, then slowed down. Possible explanations for that include the core having formed in the inner part of the disk and later migrated outwards, or the core having been depleted of planetesimals due to a giant neighbor. We further estimate the core accretion rate needed for the core to form on the same timescale as our model atmosphere, $\tau = 2.1$ Myrs:

$$\dot{M}_{c,acc}(M_c) \equiv \frac{M_c}{\tau} \tag{12}$$

For reference, we also plot a typically assumed planetesimal accretion rate, for which the random velocities of the planetesimals are of the order of the Hill velocity around the protoplanetary core (e.g., Goldreich et al. 2004). We denote this latter rate as $\dot{M}_{c,Hill}$. This is the accretion rate at the boundary between the dispersion dominated and shear dominated regimes. We estimate $\dot{M}_{c,Hill}$ following Rafikov (2006) (equation A1):

$$\dot{M}_{c,Hill} = \Omega\Sigma_p R_c R_H, \tag{13}$$

where Σ_p is the surface density of solids, assumed to satisfy $\Sigma_d \approx 100\Sigma_p$ for a dust-to-gas ratio of 0.01.

6.2. *Comparison with Standard Results*

Next, we are interested in whether hydrodynamic gas accumulation due to planetesimal accretion can already commence before the atmosphere becomes unstable due to Kelvin-Helmholtz contraction, as our regime is no longer the relevant one under such conditions. From equation (11), the planetesimal accretion rate during the atmosphere evolution has to satisfy

$$\dot{M}_c \lesssim \frac{L_{KH}R_c}{GM_c} \tag{14}$$

for our regime to be valid, i.e. $L_{acc} \lesssim L_{L_{KH}}$. The maximum planetesimal accretion rate $\dot{M}_{c,KH}$ that satisfies this condition (when $L_{acc} = L_{KH}$) is denoted by the dotted line in Figure 12 for $a = 60$ AU and $M_c = 5M_\oplus$. If unstable atmosphere collapse does not occur due to planetesimal accretion for the lowest value of $M_{c,KH}$, then runway gas accretion can only occur in the KH dominated regime. In what follows we calculate the critical core mass $M_{c,KH}$ corresponding to $\dot{M}_{c,KH}$ and show that it is higher than our calculated critical core mass.

In order to estimate $M_{c,KH}$, we use the results of Rafikov (2006) for low luminosity atmospheres forming in the outer disk ($> 2-5$ AU), consistent with our region of interest. Rafikov (2006) assumes an ideal gas polytropic equation of state and a lower opacity than the standard ISM opacity that we use in our calculations (see equation 5). We thus calculate the critical core mass for an ideal gas polytrope with the standard ISM opacity reduced by

a factor of 100, which is comparable to the opacity law used by Rafikov (2006) (see PY13).

By relating his expression for the critical core mass to a given core mass dependent planetesimal accretion rate $\dot{M}(M_c)$, we find the following expression for the critical core mass when accretion luminosity dominates the evolution of the atmosphere:

$$M_{\rm crit,KH} \sim \left[\frac{\dot{M}(M_c)}{64\pi^2 C}\frac{\kappa_0}{\sigma G^3}\frac{1}{R_c M_c^{1/3}}\left(\frac{k_b}{\mu}\right)^4\right]^{3/5}, \quad (15)$$

with all the constants as defined in previous sections, and C an order unity constant depending on the adiabatic gradient and disk properties (see Rafikov 2006, equation B3). The result is displayed in Figure 13; the critical core mass corresponding to planetesimal accretion at the rates displayed in Figure 12 is displayed for comparison.

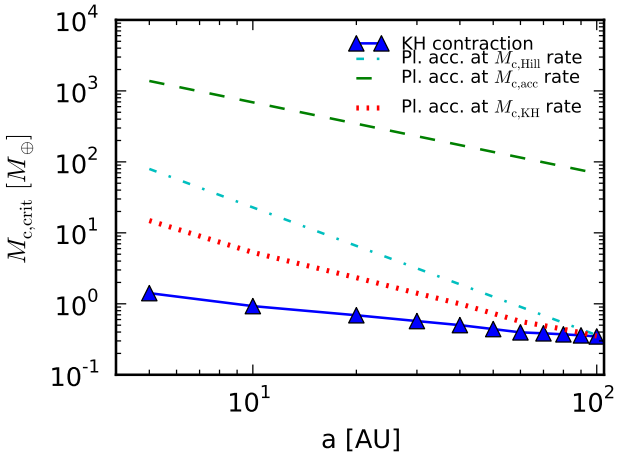

FIG. 13.— Comparison between the critical core mass $M_{\rm crit,KG}$ due to planetesimal accretion and the assumed fixed core mass when gas contraction dominates, for a growth time of $\tau = 2.1$ Myrs. Our results yield lower core masses than in the standard case.

The critical core mass due to planetesimal accretion is smaller than in the case in which planetesimal accretion dominates the evolution of the atmosphere. This brings us to two conclusions. First, we confirm that planetesimal accretion can be safely ignored in our regime of interest. Secondly, this comparison tells us that it is easier and more efficient to form a planet by growing the core first, then accreting a massive envelope, rather than by growing the core and atmosphere in parallel. Moreover, our result represents a true, absolute minimum on the core mass that is needed to form a giant planet during the lifetime of the protoplanetary disk, as our core no longer grows.

As a final check, we investigate whether planetesimal accretion during the gas contraction phase at the rate $\dot{M}_{\rm KH}$ imposed by the condition that $L_{\rm acc} < L_{\rm KH}$ can alter the core mass enough to affect the time evolution of the atmosphere. We can quantitatively estimate the increase in core mass as

$$\Delta M_c = \int_0^{t_{\rm co}} \dot{M}_c dt \approx \sum \dot{M}_{ci}\Delta t_i, \quad (16)$$

where the accretion rate $\dot{M}_{ci}$ is given by

$$\dot{M}_{ci} = \frac{L_i R_c}{G M_c} \quad (17)$$

from equation (11), with L_i the luminosity of the atmosphere at time t_i in our model. For $M_c = 10M_\oplus$, we find $\Delta M_c \approx 0.2 M_\oplus$. This mass increase is therefore negligible in comparison with the initial core mass. It follows that a significant increase in core mass that could potentially alter the time evolution of the atmosphere would occur on a longer time scale than the mass-doubling time for the unperturbed atmosphere. Therefore, the time evolution of the atmosphere is insensitive to core mass changes at a rate imposed by the assumption that $L_{\rm acc} < L_{\rm KH}$.

7. CONCLUSIONS

In this paper we have studied giant planet formation under the assumption that the planetesimal accretion rate is negligible and the atmosphere evolution is dominated by gas contraction. We have used the model developed in PY13 to build atmosphere profiles assuming that the nebular gas obeys a realistic equation of state that takes into account non-ideal effects. We found that the variations in the adiabatic index due to the realistic equation of state result in a significantly larger crossover time, and therefore critical core mass, when compared to an ideal gas polytrope. While for an ideal diatomic gas the minimum core mass to form a giant planet under the assumptions of our model is lower than the typically quoted value of $10M_\oplus$ (see Piso & Youdin in prep.), the inclusion of non-ideal effects brings this values back to around $10M_\oplus$,

We also compared our results to standard studies that assume that the evolution of the gaseous envelope is dominated by planetesimal accretion. We found that that our model yields lower core masses than the standard results. It is therefore easier to form a giant planet by growing the core first, then reducing the planetesimal accretion rate and let the atmosphere evolve on a Kelvin-Helmholtz time scale. Moreover, our results represent a true minimum on the core mass needed to form a giant planet during the typical lifetime of a protoplanetary disk.

REFERENCES

Beckwith, S. V. W. & Sargent, A. I. 1991, ApJ, 381, 250
Beckwith, S. V. W., Sargent, A. I., Chini, R. S., & Guesten, R. 1990, AJ, 99, 924
Bell, K. R. & Lin, D. N. C. 1994, ApJ, 427, 987
Bodenheimer, P. & Pollack, J. B. 1986, , 67, 391
Chiang, E. & Youdin, A. N. 2010, Annual Review of Earth and Planetary Sciences, 38, 493
D'Alessio, P., Calvet, N., & Hartmann, L. 2001, ApJ, 553, 321
D'Angelo, G., Durisen, R. H., & Lissauer, J. J. Giant Planet Formation, ed. S. Piper, 319–346
Farkas, A. 1935, Orthohydrogen, Parahydrogen and Heavy Hydrogen
Goldreich, P., Lithwick, Y., & Sari, R. 2004, ARA&A, 42, 549
Ikoma, M., Nakazawa, K., & Emori, H. 2000, ApJ, 537, 1013
Kippenhahn, R. & Weigert, A. 1990, Stellar Structure and Evolution

Kittel, C., Kroemer, H., & Landsberg, P. T. 1981, Nature, 289, 729
Mandl, F. 1989, Statistical Physics, 2nd Edition
Mizuno, H., Nakazawa, K., & Hayashi, C. 1978, Progress of Theoretical Physics, 60, 699
Papaloizou, J. C. B. & Terquem, C. 1999, ApJ, 521, 823
Pérez, L. M., Carpenter, J. M., Chandler, C. J., Isella, A., Andrews, S. M., Ricci, L., Calvet, N., Corder, S. A., Deller, A. T., Dullemond, C. P., Greaves, J. S., Harris, R. J., Henning, T., Kwon, W., Lazio, J., Linz, H., Mundy, L. G., Sargent, A. I., Storm, S., Testi, L., & Wilner, D. J. 2012, ApJ, 760, L17
Pollack, J. B., McKay, C. P., & Christofferson, B. M. 1985, , 64, 471
Rafikov, R. R. 2006, ApJ, 648, 666
Saumon, D., Chabrier, G., & van Horn, H. M. 1995, ApJS, 99, 713
Stevenson, D. J. 1982, Planet. Space Sci., 30, 755
Thompson, M. J. 2006, An introduction to astrophysical fluid dynamics
Wuchterl, G. 1993, , 106, 323

APPENDIX

EQUATION OF STATE TABLES

In this section we explain the procedure for extending and interpolating the Saumon et al. (1995) equation of state tables. The equation of state takes into account non ideal interactions, and includes physical treatments of dissociation and ionization. However, the Saumon et al. (1995) EOS tables only cover a relatively high range of temperatures and pressures: $2.10 < \log_{10} T(\mathrm{K}) < 7.06$ and $4 < \log_{10} P(\mathrm{dyn\ cm^{-2}}) < 19$. We consider cold disks, where the temperature and pressure drop to ~ 20 K and $\sim 10^{-4}$ dyn cm^{-2}, respectively (see equations (1b) and (1c)). As such, it is necessary to extend the Saumon et al. (1995) EOS tables to lower temperature and pressure values.

We choose $\log_{10} T(\mathrm{K}) = 1$ and $\log_{10} P(\mathrm{dyn\ cm^{-2}}) = -4.4$ as our lower boundaries for temperature and pressure, respectively. Our temperature and pressure grid becomes: $1 < \log_{10} T(\mathrm{K}) < 7.06$ and $-4.4 < \log_{10} P(\mathrm{dyn\ cm^{-2}}) < 19$. The other thermodynamic variables in the tables are calculated as follows.

Hydrogen

For a system of particles, the partition function can be written as the product of all partition functions associated with each type of energy that the system can have:

$$Z = Z_t Z_r Z_v Z_e Z_n, \tag{A1}$$

where Z_t, Z_r, Z_v, Z_e and Z_n are the partition functions associated with translation, rotation, vibration, electronic excitation and nuclear excitation, respectively. For hydrogen, electronic and nuclear excitation are only significant at temperatures higher than our region of interest ($\theta_e \approx 12000$ K and $\theta_n >> \theta_e$, where θ_e and θ_n are the characteristic temperatures for electronic and nuclear excitation, respectively). As such, we will only take into account the translation, rotation and vibration of the hydrogen molecule:

$$Z = Z_t Z_r Z_v \tag{A2}$$

The partition function associated with the motion of the center of mass of the molecule is given by (in the classical limit):

$$Z_t = (m/2\beta\pi\hbar^2)^{3/2} V, \tag{A3}$$

where $\beta = 1/(kT)$ and V is the volume. The rotational partition function is generally written as:

$$Z_r = \sum_0^\infty (2j+1) \exp\Big[\frac{-j(j+1)\Theta_r}{T}\Big], \tag{A4}$$

where Θ_r is the characteristic temperature for rotational motion. In the case of hydrogen, $\Theta_r \approx 85$ K. However, molecular hydrogen occurs in two isomeric forms: orthohydrogen, with the proton spins aligned parallel to each other, and parahydrogen, with the proton spins aligned antiparallel. Parahydrogen can only a have symmetric (even) wave function associated with rotation, while orthohydrogen can only have an antisymmetric (odd) wave function associated with rotation (see section 3 for an explanation why). The rotational partition functions for ortho- and parahydrogen can thus be written as:

$$Z_{\mathrm{r,para}} = \frac{1}{2} \sum_0^\infty (1 + (-1)^j)(2j+1) \exp\Big[-\frac{j(j+1)\Theta_r}{T}\Big] \tag{A5}$$

and

$$Z_{\mathrm{r,ortho}} = \frac{3}{2} \sum_0^\infty (1 - (-1)^j)(2j+1) \exp\Big[-\frac{j(j+1)\Theta_r}{T}\Big] \tag{A6}$$

The factor of 3 above accounts for the three-fold degeneracy of the ortho state.

When the two isomers are in equilibrium, the combined partition function is given by the sum of the individual partition functions, $Z_{\rm r} = Z_{\rm r,ortho} + Z_{\rm r,para}$ and can be written as:

$$Z_r = \sum_0^\infty (2-(-1)^j)(2j+1)\exp\Big[\frac{-j(j+1)\Theta_r}{T}\Big] \tag{A7}$$

In our range of temperatures of interest, we found that Z_r converges after about 25 terms in the series.

Finally, the partition function for vibrational motion is given by:

$$Z_v = [1-\exp(\theta_v/T)]^{-1}, \tag{A8}$$

where θ_v is the characteristic temperature for vibrational motion, $\theta_v \approx 6140$ K for hydrogen.

If the partition function of a system of N particles is known in terms of (V,T,N), the internal energy and entropy of the system can be determined as follows:

$$U_N = kT^2\Big(\frac{\partial \log Z}{\partial T}\Big)_{V,N} \tag{A9}$$

$$S_N = k\log Z + \frac{U_N}{T} \tag{A10}$$

The energy, and entropy per mass and specific heat capacity will subsequently be:

$$U = \mathcal{R}T^2\Big(\frac{\partial \log Z}{\partial T}\Big)_{V,N} \tag{A11}$$

$$S = \mathcal{R}\log Z + \frac{U}{T} \tag{A12}$$

$$C_v = \Big(\frac{\partial U}{\partial T}\Big)_{V,N} \tag{A13}$$

Since $Z = Z_t Z_r Z_v$, it is easy to notice that $U = U_t + U_r + U_v$ and $S = S_t + S_r + S_v$, where U_t, U_r, U_v, S_t, S_r, S_v are the quantities corresponding to the individual translation, rotation and partition functions, respectively.

It can be shown that the entropy per mass due to translational motion can be expressed as:

$$S_t = \mathcal{R}\Big[\frac{5}{2}\ln T - \ln P + \ln\Big(\frac{(2\pi)^{3/2}\mathcal{R}^{5/2}\mu^4}{h^3}\Big) + \frac{5}{2}\Big] \tag{A14}$$

with μ the mean molecular weight. Equation (A14) is known as the Sackur-Tetrode formula, and it is only applicable to an ideal gas. It can also be easily shown that the internal energy per mass due to translational motion is given by:

$$U_t = \frac{3}{2}\mathcal{R}T \tag{A15}$$

Putting all of the above together, we can now evaluate the thermodynamic quantities needed to extend the Saumon et al. (1995) EOS tables to low temperatures and pressures.

1. **Density.** In the low temperature, low pressure regime, hydrogen is molecular and behaves like an ideal gas. As such, the density in this region follows the ideal gas law $P = \rho\mathcal{R}T$.
2. **Internal energy per mass.** $U = U_t + U_r + U_v$, where U_t is given by equation (A15), and U_r, U_v are determined using equations (A11), (A7) and (A8) above.
3. **Entropy per unit mass**. Similarly, $S = S_t + S_r + S_v$, where S_t is given by equation (A14), and S_r, S_v can be determined from equation (A12) and the calculated expressions for U_r and U_v, respectively.
4. **Entropy logarithmic derivatives**. The logarithmic derivatives S_T and S_P are given by:

$$S_T = \frac{\partial \log S}{\partial \log T}\Big|_P \tag{A16}$$

and

$$S_T = \frac{\partial \log S}{\partial \log P}\Big|_T \tag{A17}$$

We calculate S_T and S_P using the table values for S, T and P, and a linear central difference formula.

5. **Adiabatic gradient** ∇_{ad}. The adiabatic gradient is defined as:

$$\nabla_{ad} = \frac{\partial \log T}{\partial \log P}\Big|_S = -\frac{S_P}{S_T} \tag{A18}$$

We evaluate it from the tabulated values for S_T and S_P determined above. Figure 1 shows a contour plot of the adiabatic index for the extended EOS table, while the black lines represent constant entropy curves. The upper right part of the plot ($\log T > 2.1$ and $\log P > 4$) is based on the Saumon et al. (1995) EOS table, while the rest of the plot is our extension. We see that the two tables join smoothly for entropy curves between $8.80 < \log S(\mathrm{K\ g^{-1}}) < 9.07$.

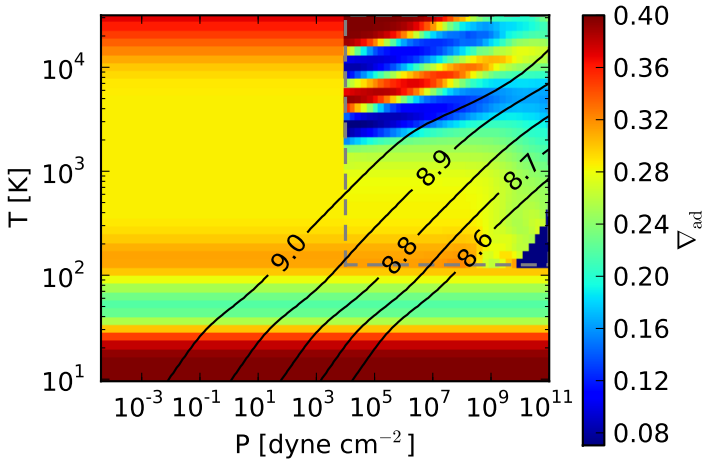

FIG. 14.— Contour plot of the adiabatic gradient $\nabla_{\rm ad}$ for the hydrogen extended table. The black curves represent constant entropy curves.

Helium

We extend the helium EOS tables based on a similar procedure. Since helium is primarily neutral and atomic at low temperatures and pressures, we treat it as an ideal monoatomic gas, and subsequently only take into account the translational components of the necessary thermodynamic quantities (see subsection A.1 above for details). The analogous ∇_{ad} contour plot for helium can be seen in Figure 2. We notice that, in the case of helium, the original and extended table join smoothly for entropy curves between $8.29 < \log S(\mathrm{K\ g^{-1}}) < 8.77$.

Lastly, we obtain the equation of state tables for the hydrogen-helium mixture thorough the procedure described in Saumon et al. (1995), for a helium mass fraction $Y = 0.3$.

ADIABATIC GRADIENT DURING PARTIAL IONIZATION

For a partially ionized gas, the total internal energy includes contributions from the individual internal energies of neutral atoms, ions and electrons, as well as from the ionization energy. Specifically, if we denote the internal energies of neutral hydrogen, protons and electrons as U_H, U_+ and U_e, respectively, then the total internal energy of the gas is given by:

$$U = U_H + U_+ + U_e + x\chi, \tag{B1}$$

where x is the ionization fraction and χ is the ionization energy (equal to -13.6 eV for hydrogen). The ionization fraction can be determined from the Saha equation (see e.g., Kippenhahn & Weigert 1990).

$$\frac{x^2}{1-x}\frac{\rho}{m_H} = \frac{(2\pi m_e k_B T)^{3/2}}{h^3} e^{-\chi/k_B T}, \tag{B2}$$

where m_e is the mass of the electron and h is Planck's constant. It can be seen from the Saha equation that the ionization fraction depends only on the gas temperature and density: $x = x(T, \rho)$. As such, all the thermodynamic quantities also depend only on the gas temperature and density, and hence on the equation of state. The adiabatic gradient is given by (see Kippenhahn & Weigert 1990, chapter 14 for a derivation):

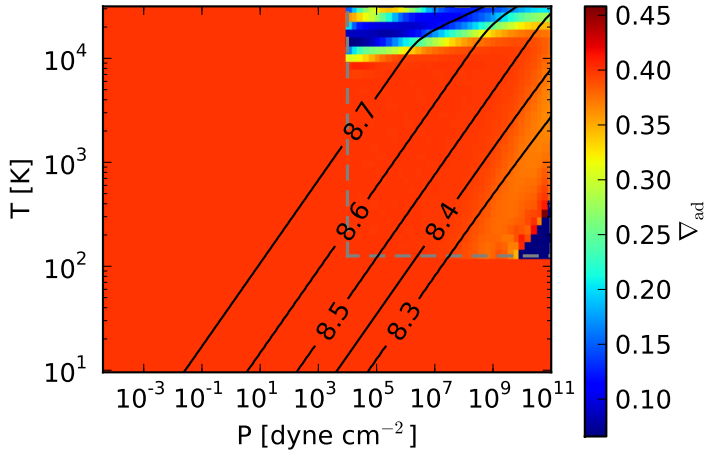

FIG. 15.— Contour plot for the adiabatic gradient ∇_{ad} for the helium extended table. The black curves represent constant entropy curves.

$$\nabla_{ad} = \frac{2 + x(1-x)\Phi_H}{5 + x(1-x)\Phi_H^2}, \tag{B3}$$

with $\Phi_H = \frac{5}{2} + \frac{\chi}{kT}$. Figure 16 shows the behavior of ∇_{ad} for partially ionized hydrogen. We recover $\nabla_{ad} = 2/5$ for $x = 0$ (pure atomic hydrogen) and $x = 1$ (fully ionized plasma). The adiabatic gradient decreases significantly for intermediate values of x, becoming smaller than 0.1 at its minimum (for $x = 0.5$).

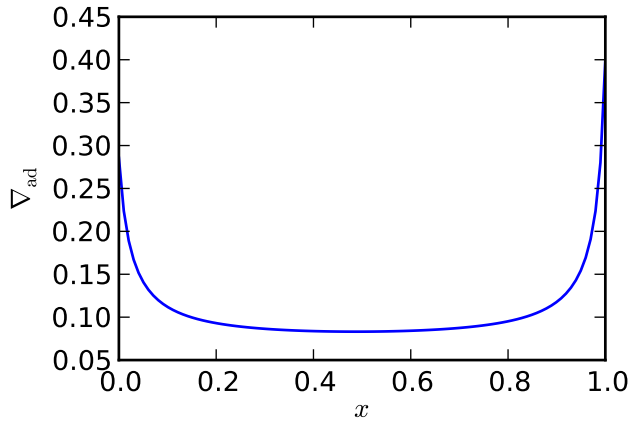

FIG. 16.— Adiabatic gradient as a function of the hydrogen ionization fraction x. The adiabatic gradient is $\nabla_{ad} = 2/5$ for pure atomic hydrogen ($x = 0$) and fully ionized hydrogen ($x = 1$), and drops to low values during partial ionization.

RADIATIVE WINDOWS

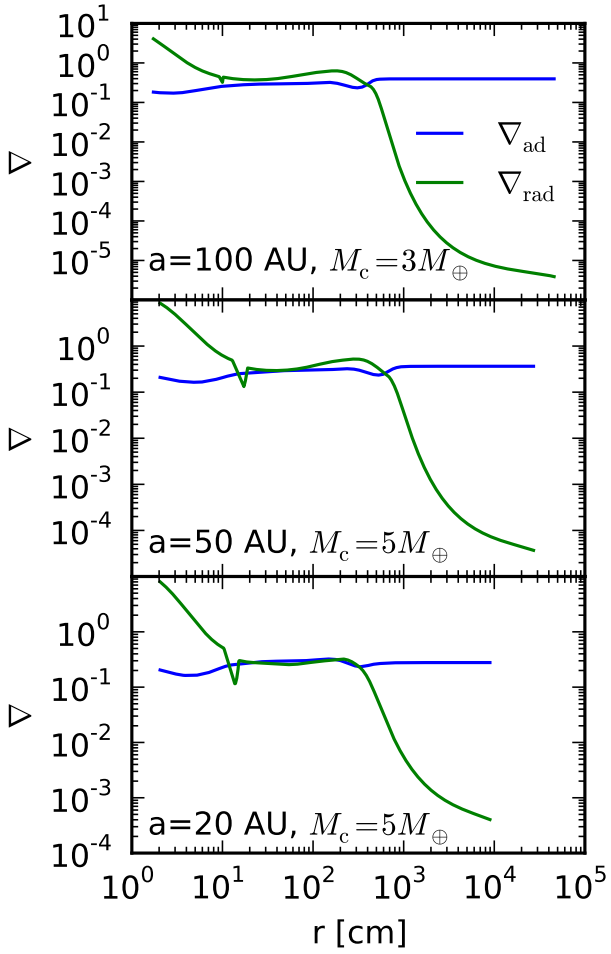

FIG. 17.— Radiative and adiabatic gradient as a function of radius. The sharp drom in opacity due to dust sublimation can generate one or more radiative windows.

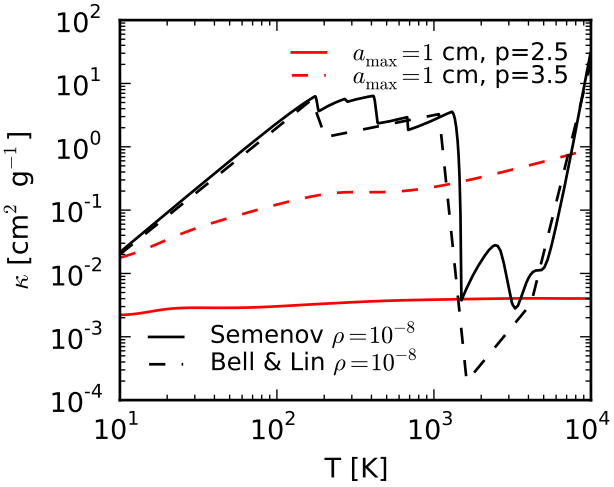

FIG. 18.— Opacities...